RESEARCH ARTICLE

INTERNATIONAL RESEARCH JOURNAL OF MULTIDISCIPLINARY TECHNOVATION

Asian Research Association

DOI: 10.54392/irjmt26419

Growth, Structural Characterization, and Nonlinear Optical Properties of L-Lysinium Hydrogen Adipate Single Crystals: An Integrated Experimental and DFT Study

R. Thirumurugan [a, *], Srirengaraj Vijayaram [b], E. Shobhana [c], V. Mohanraj [d]

[a] Department of Physics, Easwari Engineering College, Chennai-600089, Tamil Nadu, India.
[b] Department of Biotechnology, Karpagam Academy of Education, Coimbatore-641021, Tamil Nadu, India.
[c] Department of Physics, Kumaraguru College of Technology, Coimbatore-641049, Tamil Nadu, India.
[d] Division of Chemical Sciences, Tamil Nadu State Council for Science and Technology, DOTE Campus, Chennai-600025, Tamil Nadu, India.

* Corresponding Author Email: beblissful006@gmail.com

DOI: https://doi.org/10.54392/irjmt26419

Received: 04-09-2025; Revised: 02-06-2026; Accepted: 18-07-2026; Published: 27-07-2026

Abstract: The proton-transfer salt L-lysinium hydrogen adipate (LLA) was obtained as single crystals by slow evaporation from an aqueous solution at room temperature. It comprises the natural amino acid L-lysine in its cationic form together with adipic acid as the diacid component. LLA crystallizes in the non-centrosymmetric (NCS) monoclinic space group $P2_1$, the symmetry required for bulk second-harmonic generation (SHG). Powder XRD confirmed phase purity. Hirshfeld surface analysis quantified the intermolecular contacts that stabilize the NCS packing, showing that N–H···O and O–H···O hydrogen bonds together contribute 45.8% of the Hirshfeld surface area. The Kurtz–Perry powder method showed an SHG efficiency 1.2 times that of potassium dihydrogen phosphate (KDP) under Q-switched Nd:YAG laser excitation (λ = 1064 nm). The LLA crystal exhibits thermal stability up to 150 ºC and a distinct melting endotherm at 203 ºC. Density functional theory (DFT) calculations at the B3LYP/6-31+G (d,p) level yielded a HOMO-LUMO gap of 5.34 eV, indicating favourable electronic and charge-transfer characteristics for NLO behaviour. Natural bond orbital (NBO) analysis attributed the NLO response primarily to LP→π*/σ* interactions at the carboxylate termini ($E^{(2)}$ up to 113.03 kcal mol^{-1}). The calculated first hyperpolarizability (β_{total} = 460.79 × 10^{-30} esu, approximately 795 times that of urea) is consistent with the experimental SHG efficiency. Taken together, the experimental and computational results position LLA as a viable organic material for frequency-doubling and photonic device applications.

Keywords: L-Lysinium Hydrogen Adipate, Nonlinear Optical Materials, Single-Crystal XRD, DFT Studies, NBO Analysis, Hyperpolarizability, Hirshfeld Surface Analysis.

1. Introduction

The need for compact, efficient optical frequency converters and electro-optic modulators for use in telecommunications, laser technology, and integrated photonics has fueled the search for organic and semi-organic nonlinear optical (NLO) materials over the last two decades [1, 2]. Although inorganic benchmarks such as KDP and $LiNbO_3$ provide well-characterized performance, they also suffer from limitations such as challenging crystal growth and stringent phase-matching bandwidths [3]. By comparison, organic crystals can be designed at the molecular level to exhibit large first hyperpolarizability (β), and their typically softer crystal lattices allow phase matching of SHG over a wider wavelength range [4].

Proton-transfer salts constructed from amino acids are particularly attractive intermediate-sized compounds in organic NLO crystal engineering [5]. Their intrinsic chirality removes the inversion symmetry that quenches second-order $\chi^{(2)}$, while the extensive hydrogen-bond networks typical of amino acid salts enforce rigid polar supramolecular architectures in which the hyperpolarizability of individual molecules is translated into a macroscopic NLO response [6]. This behaviour is especially well realized in the amino acid L-lysine: its two amino groups (α-NH_2 and ε-NH_2) provide several potential protonation sites and strong hydrogen-bond donors, which, in combination with a dicarboxylic acid anion, can generate a dense network of N−H···O and O−H···O contacts that constrain the crystal into an NCS structure [7]. Several L-lysine complexes with carboxylic acids have previously been studied, among

which the tartrate [7] and maleate [8] salts showed SHG activity. Adipic acid (hexanedioic acid) is a flexible, symmetric diacid whose six-carbon aliphatic chain can adopt diverse conformations, allowing it to bridge lysinium cations in a manner that optimizes the alignment of dipolar $NH3^{+}\cdots{}^{-}OOC$ charge-transfer vectors [9]. Earlier crystallographic studies of lysine adipate reported the NCS $P2_1$ space group [10], but a comprehensive structure-property analysis linking the supramolecular architecture to NLO performance through Hirshfeld surface analysis and DFT-level electronic-structure calculations has not been reported. This gap is significant because, without a quantitative analysis of orbital interactions and charge distribution, the rational optimization of adipate chain length and substitution pattern for enhanced β remains speculative [11].

The present work addresses this gap by growing LLA single crystals through slow evaporation and systematically characterizing them using SCXRD, powder XRD, Hirshfeld surface analysis, thermal analysis, and Kurtz-Perry SHG measurements. At the B3LYP/6-31+G (d,p) level, DFT calculations provide HOMO-LUMO topologies, molecular electrostatic potential (MEP) maps, Mulliken charge distributions, NBO donor-acceptor stabilization energies, and first-hyperpolarizability tensors. The study has three goals: to provide a quantum-mechanically consistent explanation of the measured SHG efficiency, to identify the orbital pathways responsible for charge transfer, and to show that the ion-pair architecture of a simple amino-acid salt can produce second-order nonlinearity that is greater than or comparable to that of extended π-conjugated systems.

2. Experimental

2.1 Crystal Growth

L-lysine (Sigma-Aldrich, ≥98%) and adipic acid (Sigma-Aldrich, ≥99.5%) were dissolved in equimolar amounts in deionized water at room temperature under magnetic stirring until a clear solution was obtained (Figure 1a). The solution was filtered through Whatman No. 1 filter paper to remove insoluble particulates and then poured into a covered glass Petri dish. The evaporation process was allowed to proceed slowly at room temperature (25 ± 1 °C) under dust-free conditions. Within 8–12 days, good-quality, colorless, transparent crystals suitable for single-crystal X-ray diffraction became visible. The harvested crystals (Figure 1b) were rinsed with cold deionized water, air-dried under ambient conditions for 2–16 h, and then used for characterization.

2.2 Experimental Methods

Data were collected using a Bruker APEX-II CCD diffractometer with graphite-monochromated Mo Kα radiation (λ = 0.71073 Å) at 293 K. Selected crystals were carefully crushed to prepare polycrystalline powder. Powder XRD patterns were recorded over the 2θ range 5°–60°, using a step size of 0.02° and a scan speed of 2° min^{-1}, with Cu Kα radiation (λ = 1.54056 Å) on a Rigaku MiniFlex 600 diffractometer. Phase purity was confirmed by comparing the experimental data with simulated patterns generated from the CIF file in Mercury 4.0 using the SCXRD structure (Figure. 2). TGA and DTA were performed simultaneously on a PerkinElmer STA 6000.

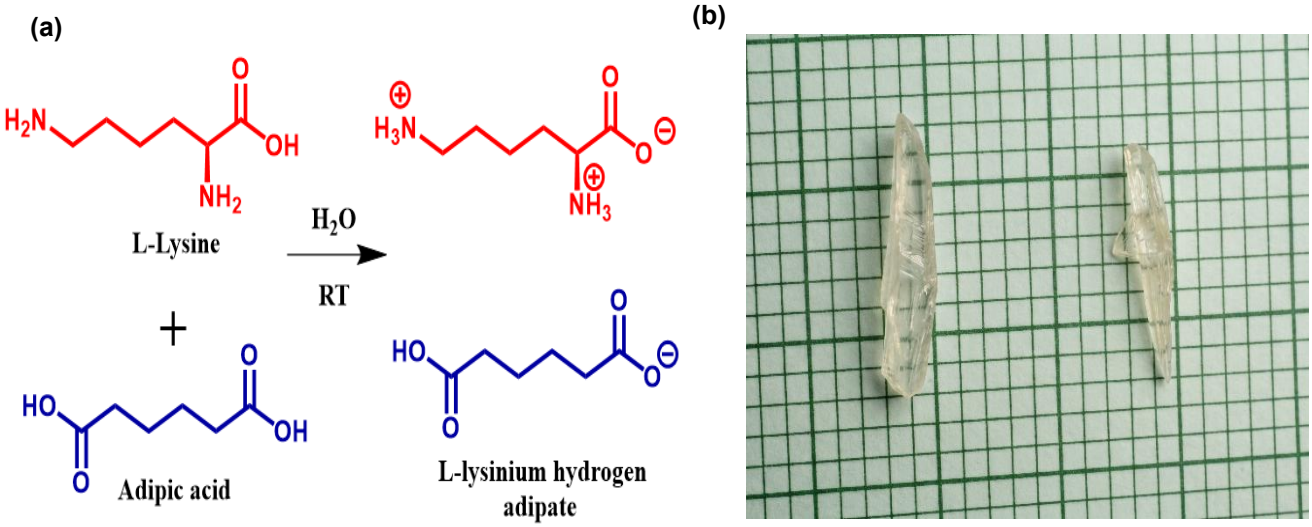

Figure 1. (a) Chemical scheme of LLA, **(b)** Photograph of as grown LLA crystal.

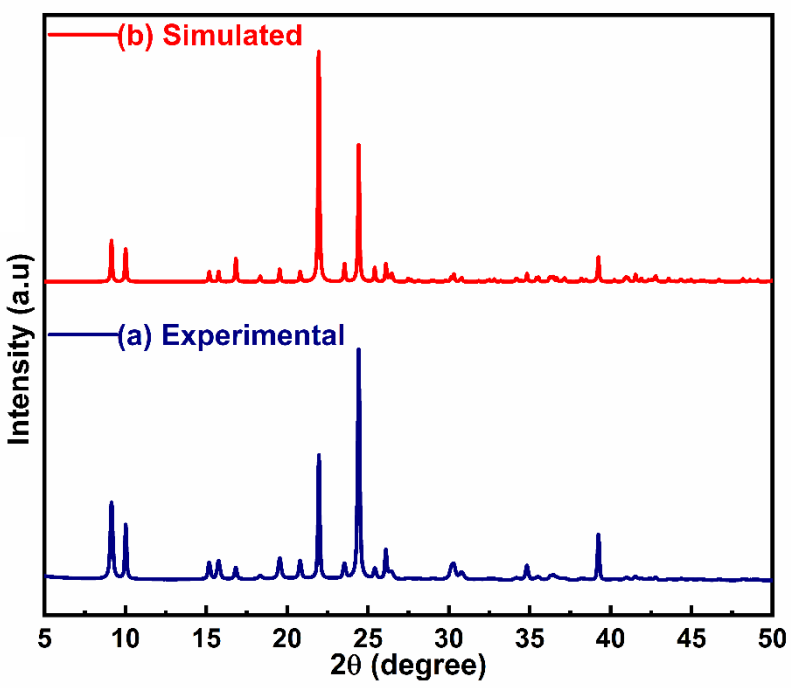

Figure 2. (a) Experimental (lower) and **(b)** simulated (upper) powder XRD patterns of LLA.

A mass of about 5 mg was placed in an alumina crucible and heated from 30 to 600 °C at a rate of 10 °C min^{-1} under a nitrogen atmosphere with a flow rate of 20 mL min^{-1}; empty alumina crucibles served as references. The SHG efficiency of powdered LLA was measured using a Q-switched Nd:YAG laser (λ = 1064 nm, pulse width 10 ns, repetition rate 10 Hz, pulse energy ≈ 5.7 mJ) and the modified Kurtz-Perry technique [12].

The powdered sample was sieved to a particle size of 120–150 μm. The frequency-doubled output at 532 nm was isolated from the fundamental beam with a BG-38 bandpass filter and a Jobin-Yvon monochromator, and detected by a Hamamatsu R2059 photomultiplier tube connected to a 500 MHz digital oscilloscope (Tektronix TDS 3052B). Commercial potassium dihydrogen phosphate (KDP), ground to the same particle size, was used as the reference standard. All SHG outputs are expressed as ratios of the peak-to-peak signal voltages measured under identical beam conditions.

3. Computational Methodology

Using Gaussian 09 (Revision D.01) on an Intel Core i7 (3.40 GHz) workstation, the geometry of the LLA ion pair was optimized at the B3LYP/6-31+G (d,p) level, with no symmetry constraints imposed [13]. The total energy of the optimized system was −476.088 a.u. Frontier molecular orbital (FMO) energies, Mulliken atomic charges, and the molecular electrostatic potential (MEP) surface were computed from the converged wavefunction and visualized in GaussView 6.0 (isovalue 0.02 a.u. for FMOs; MEP electron-density isosurface 0.001 a.u.) [14]. Second-order perturbation energies E(2) were obtained through natural bond orbital (NBO) analysis using the NBO 3.1 subroutine included in Gaussian 09. The dipole moment (μ), polarizability (α), and first hyperpolarizability (β) components were determined analytically, and the scalar total β was calculated as follows: $\beta_{total} = (\beta_x^2 + \beta_y^2 + \beta_z^2)^{1/2}$. The relation 1 a.u. = 8.6393 × 10^{-33} esu was used to convert all β values into esu, where a.u. denotes the atomic unit of charge. Urea (β = 0.58 × 10^{-33} esu) was used for comparison at the same level of theory.

4. Results and Discussion

4.1 Crystal Structure and Non-Centrosymmetric Packing

The unit-cell parameters determined in this work agree well with the previously reported crystal structure (Table 1), within 0.003 Å and 0.01° for all metric parameters, confirming successful reproduction of the same polymorph. LLA is monoclinic and adopts the polar, NCS space group $P2_1$, which provides the symmetry required for bulk second-order NLO activity. The asymmetric unit consists of one lysinium cation and one adipate anion linked through proton transfer: the positively charged ε-amino group of L-lysine donates H^+, while adipic acid provides the carboxylate acceptor sites (pK_{a1} > 4.4), resulting in zwitterionic $NH_3^+\cdots OOC$ charge-transfer pairs [10]. Under the crystallization conditions, the α-amino group is also protonated (pK_a ≈ 9.0), so the lysinium cation contains two ammonium centers. Together, these features generate a robust hydrogen-bond network that sustains the $P2_1$ packing.

Table 1. Crystallographic parameters and structure refinement data for LLA.

Parameter	Literature [10]	Present work
Crystal system	Monoclinic	Monoclinic
Space group	$P2_1$	$P2_1$
a (Å)	10.532 (3)	10.530 (2)
b (Å)	7.2834 (17)	7.282 (2)
c (Å)	10.599 (3)	10.597 (3)
β (°)	113.352 (3)	113.36 (2)
V (Å³)	746.438 (3)	746.4 (2)
Z	2	2
Space group class	NCS	NCS

Arrangements of N–H···O and O–H···O bonds that break inversion symmetry direct the molecular dipoles along the polar b-axis, leading to a net macroscopic polarization [15]. Comparison with the isostructural tartrate [7] and maleate [8] complexes of L-lysinium, both of which crystallize in $P2_1$ and exhibit SHG efficiencies between 1.0 and 1.5 × KDP, indicates that the aliphatic adipate spacer provides an optimal inter-ionic geometry for phase-matched frequency doubling while avoiding the steric congestion that can limit hyperpolarizability in aromatic acid salts.

4.2 Powder XRD and Phase Confirmation

The experimental PXRD pattern of LLA is identical to the calculated pattern based on the CIF file derived from single-crystal X-ray diffraction data, with no additional reflections or peak shifts (Figure. 2). In addition, all observed Bragg reflections can be indexed to the monoclinic $P2_1$ cell, indicating that the bulk-crystallized powder is phase-pure and free from unreacted starting materials or polymorphic contaminants. The low background signal and the well-defined diffraction peaks point to very high crystallinity, consistent with the absence of a broad amorphous halo. Such phase purity is essential for reproducible SHG measurements, because mixed-phase samples can quench or distort the Kurtz-Perry signal and thereby obscure the intrinsic NLO efficiency.

4.3 Thermal Stability

The TG-DTA profile of the LLA single crystal (Figure. 3) shows significant thermal stability up to 150 ºC, with less than 2% mass loss below 100 ºC due to surface-adsorbed moisture, which appears as a small endothermic peak at 51 ºC. An initial decomposition region between 150 and 260 ºC corresponds to the sharp endothermic peak at 203 ºC, taken as the onset of melting. After melting, the TG curve shows two additional degradation steps between 260 and 630 ºC, corresponding to exothermic DTA peaks at 410 and 580 ºC that arise from oxidative cleavage of the adipate carboxylate/alkyl backbone and the lysine α-/ε-amino and carboxylate groups, respectively, before carbonization and combustion of the organic framework [16]. The negligible residual mass (≤0.4 wt% above 600 ºC) demonstrates that the salt decomposes almost quantitatively under thermo-oxidative conditions without leaving any inorganic residue, confirming that it is a purely organic amino acid-dicarboxylate salt system. The wide thermal stability window (up to ~150 ºC, well above ambient and typical device-operating conditions), combined with a sharp congruent melting endotherm at 203 ºC indicative of high crystalline purity, favours LLA for nonlinear optical, optoelectronic, and pharmaceutical applications. Moreover, the robust, charge-assisted, hydrogen-bonded ionic lattice underlying these transitions provides the structural integrity required for device-grade single-crystal performance [17].

4.4 SHG Efficiency

In the Kurtz-Perry experiment, LLA powder (120–150 μm) generated an SHG signal of 43 mV at 532 nm under 1064 nm irradiation, compared with 34 mV for KDP under identical beam conditions, yielding an SHG efficiency of 1.2 × KDP (Figure. 4). This result places LLA within the range reported for structurally related L-lysinium dicarboxylate salts (1.0–1.8 × KDP) [7, 8] and demonstrates that the aliphatic adipate anion supports efficient frequency doubling despite the absence of extended π-conjugation. Three factors appear to converge to produce this SHG response. First, the $P2_1$ space group ensures that the molecular dipoles contribute constructively to the macroscopic $\chi^{(2)}$ any centrosymmetric impurity phase would dilute the signal, but the PXRD data confirm phase purity [18]. Second, the proton-transfer structure possesses a very large ground-state dipole moment (μ_0 = 42.95 D, mainly along the x-axis), and the in-phase alignment of the unit cells provides sufficient bulk polarization for efficient phase-matched SHG near 1064 nm [19].

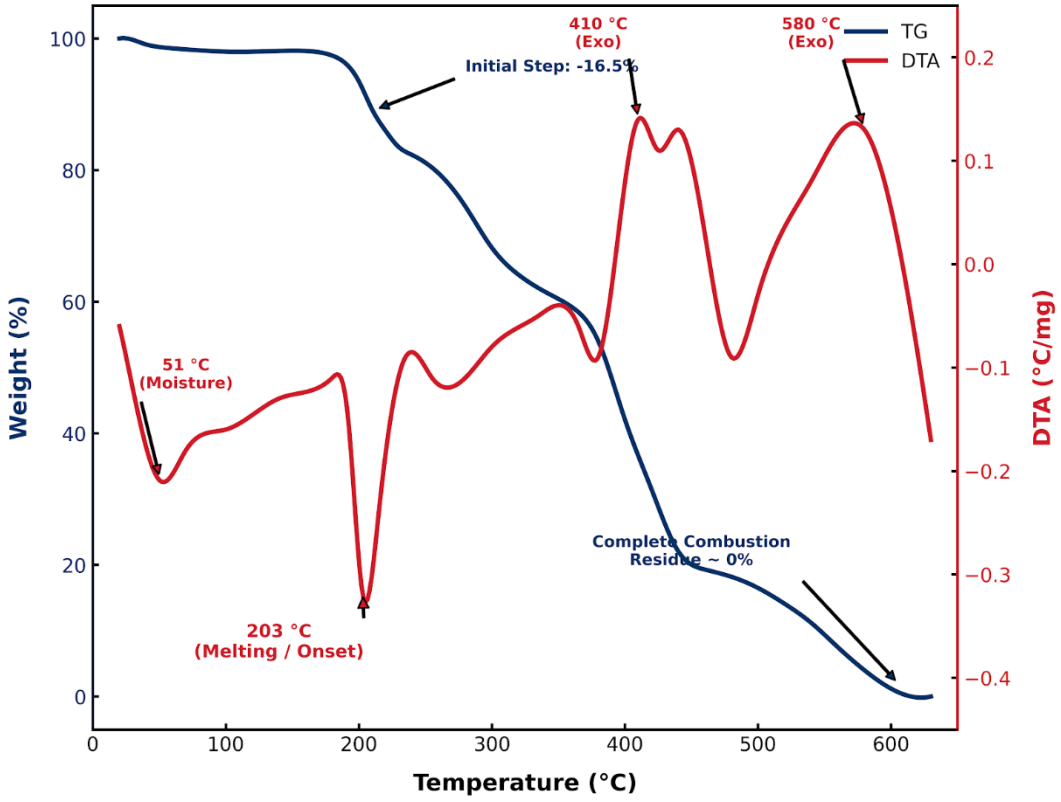

Figure 3. TG-DTA curve of LLA crystal.

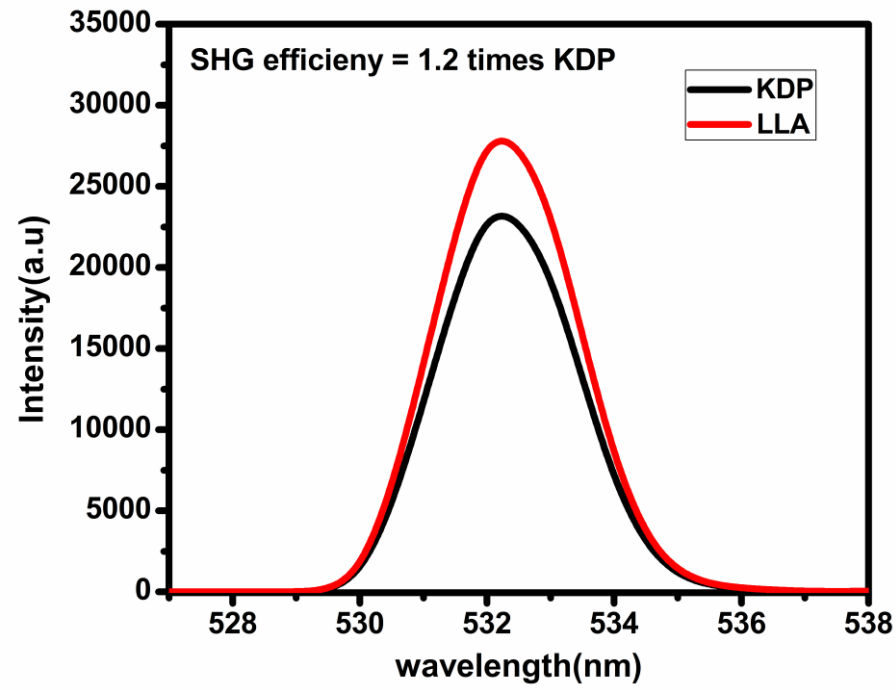

Figure 4. The powder SHG signals of KDP (black colour) and LLA (red colour).

Third, the DFT-calculated β_{total} = 460794.38 × 10^{-33} esu is approximately 795 times that of urea, indicating a hyperpolarizability driven primarily by ionic charge separation rather than by conjugation [20]. The marked enhancement in hyperpolarizability can be attributed to strong donor-acceptor interactions between the protonated lysinium cation and the hydrogen adipate anion, the substantial extent of hydrogen-bond-assisted charge transfer, and the highly polar ionic nature of the molecular framework [21]. The role of the adipate methylene spacer is also noteworthy: the conformational flexibility of the –$(CH_2)_4$– chain allows the two carboxylate termini to adopt orientations that maximize the projection of the molecular dipole onto the polar axis, thereby enhancing both the coherent addition of

molecular contributions and the powder phase-matching efficiency [22].

4.5 Hirshfeld Surface Analysis

Hirshfeld surface (HS) analysis and two-dimensional fingerprint plots were computed using CrystalExplorer 21.5 [23] from the SCXRD-refined structure to quantify and visualize the intermolecular contacts responsible for crystal packing. The HS mapped with d_{norm} (Figure. 5) displays prominent red spots above and below the carboxylate oxygen atoms, identifying them as the primary sites of short intermolecular contacts, namely the donor-to-acceptor hydrogen-bond interactions N–H···O and O–H···O. A classification of HS area contributions is provided in Table 2. The dominant H···H contacts (49.2%) reflect efficient close packing of the aliphatic methylene groups of both lysinium and adipate, stabilized by London dispersion forces. Although the H···H interactions (Figure 6) are non-directional, their high fraction indicates that the crystal is efficiently packed with a low void volume, a feature associated with good solid-state mechanical hardness and thermal stability [24]. The combined O···H and H···O contributions (35.0% + 10.8% = 45.8%) arise from the expected directional N–H···O and O–H···O hydrogen bonds. These appear in the fingerprint plot as sharp peaks at low $d_e + d_i$ values (~2.0–2.2 Å), indicative of short, strong hydrogen bonds. The asymmetry between the O···H (35.0%) and H···O (10.8%) percentages reflects the larger number of oxygen lone-pair acceptors, as adipate contributes four carboxylate/carboxyl oxygens, relative to the available N–H and O–H donors. From a design perspective, the hydrogen-bond network, which constitutes nearly half of the Hirshfeld surface, locks the NH_3^+ and COO^- dipoles into the acentric arrangement required for SHG [25]. The weak C···H contacts (3.5% combined) provide secondary stabilization through C–H···O interactions between adipate carbonyl oxygens and lysinium methylene protons (Figure 7). Although individually weak ($E^{(2)} \approx 1.44$ kcal mol^{-1} from NBO analysis), these contacts contribute to the three-dimensional cohesion of the lattice and, crucially, favour the polar packing geometry over a centrosymmetric alternative. This observation reinforces the crystallographic principle that directional, asymmetric hydrogen-bond networks are more effective than purely dispersive interactions in enforcing NCS space groups in organic salts.

Table 2. Hirshfeld surface area contributions of intermolecular contacts in LLA

Contact type	% HS area	Structural role
H···H	49.2	Dominant van der Waals packing; fills crystal voids
O···H / H···O	35.0 + 10.8 = 45.8	Primary N–H···O and O–H···O hydrogen bonds; structural directors
C···H / H···C	2.5 + 1.0 = 3.5	C–H···O contacts; secondary packing stabilization

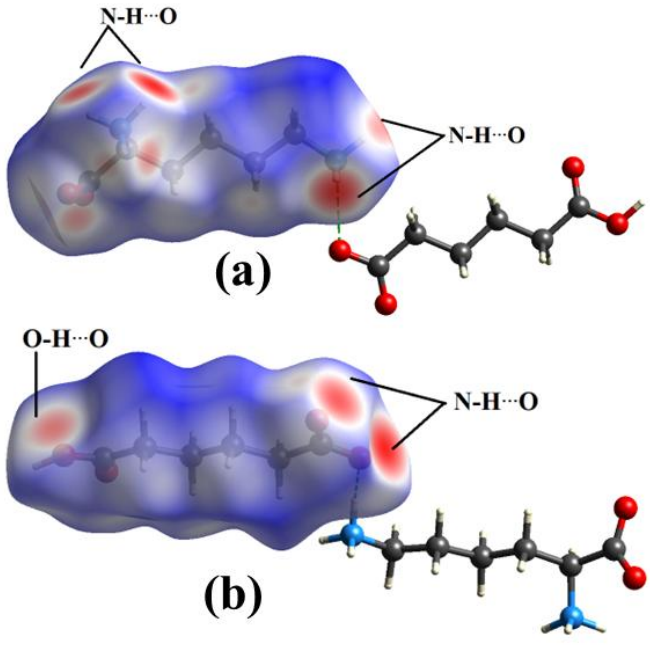

Figure 5. Hirshfeld surface of LLA mapped with d_{norm} (range −0.8 to 1.05 Å); red spots identify short N–H···O and O–H···O contacts.

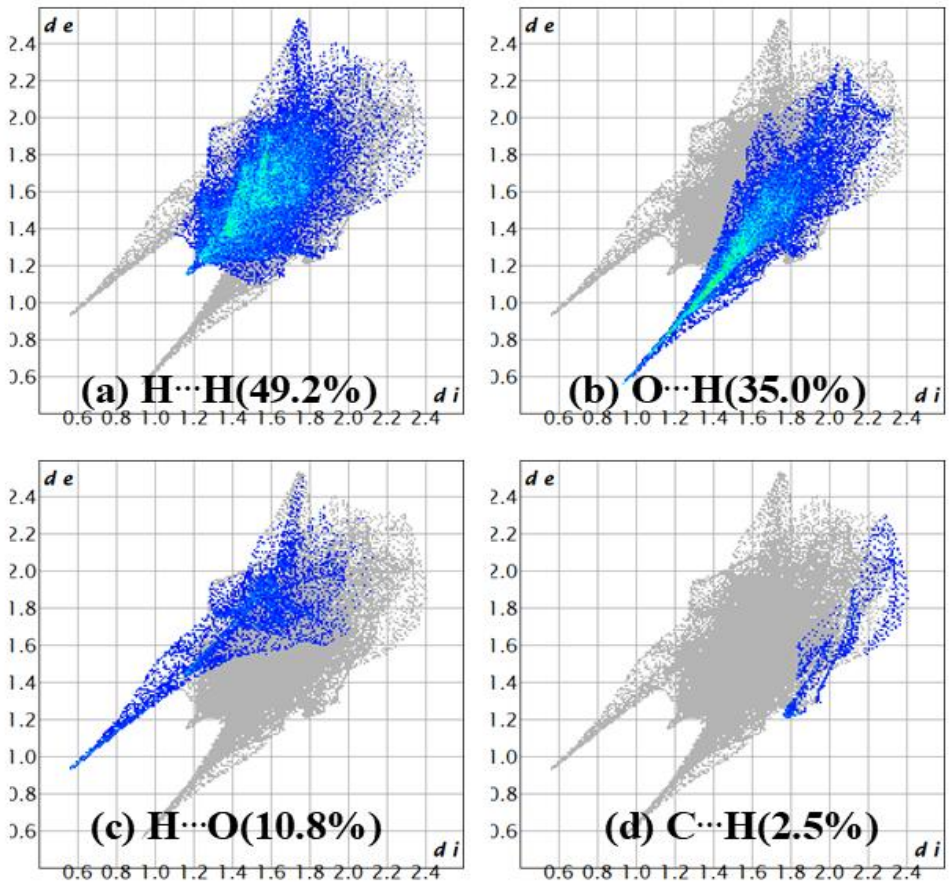

Figure 6. Fingerprint plots of **(a)** H···H (49.2 %), **(b)** O···H (35.0 %), **(c)** H···O (10.8 %), and **(d)** C··H (2.5 %), interactions.

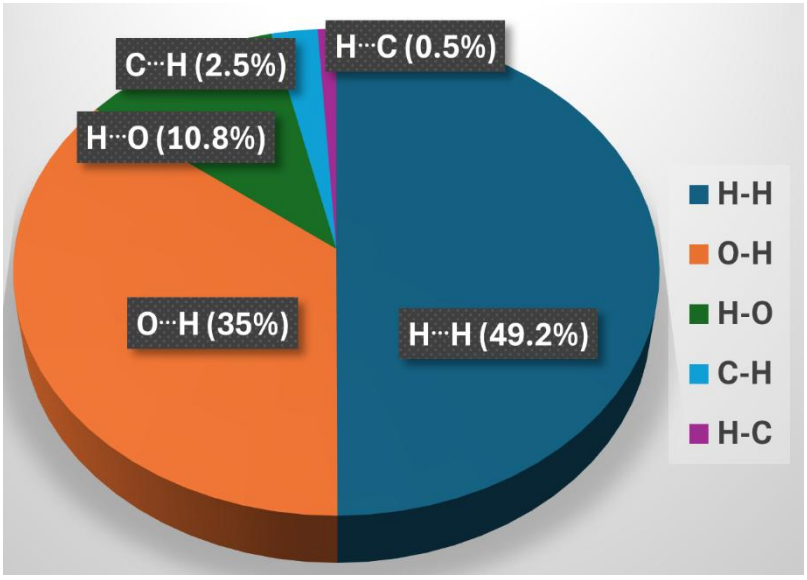

Figure 7. Percentage of intermolecular interactions involved in LLA crystal calculated using Hirshfeld surface area analysis.

4.6 DFT Computational Analysis

4.6.1 Optimized Geometry

The XRD and DFT bond lengths are in overall good agreement, generally within 0.03 Å, with the largest differences observed for the carboxylate C–O bonds. For C13–O12, the bond length changes from 1.263 Å in XRD (Table S1) to 1.346 Å in DFT, corresponding to a difference of 0.08 Å. The same carbon exhibits asymmetry in both methods (C13–O11 = 1.195 Å vs C13–O12 = 1.263 Å in XRD), although this asymmetry is not reproduced as clearly by DFT.

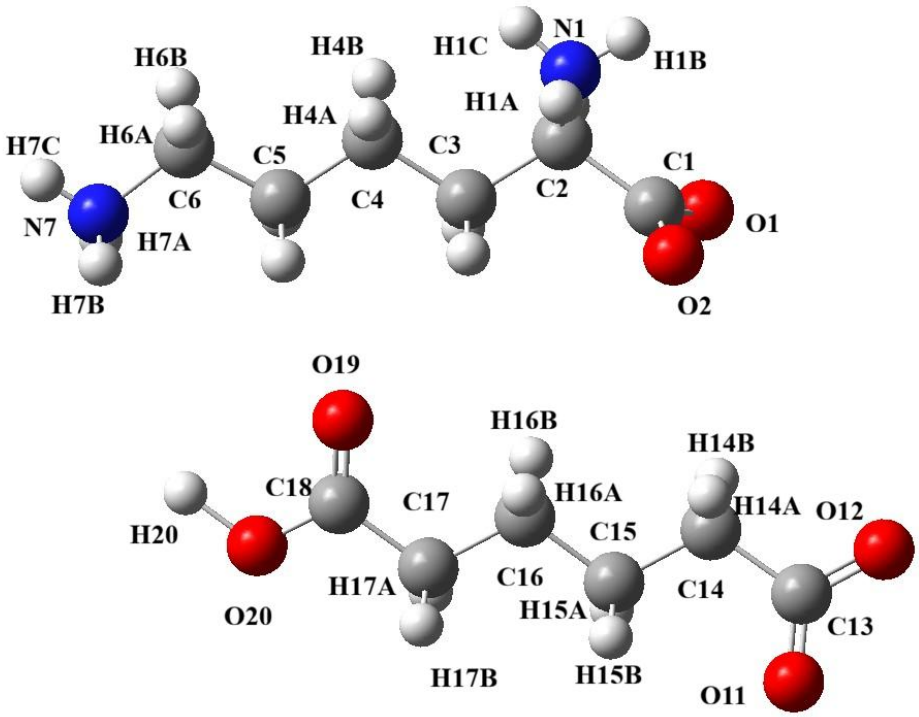

Figure 8. Optimized molecular geometry of LLA molecule.

Such structural features are consistent with the directional N–H···O and short, symmetric O–H···O hydrogen bonds previously reported for this complex [10]. Bond angles are also closely aligned, although the O–C–O angles are larger in the DFT model. For example, the O1–C1–O2 angle is 123.6º in the XRD structure (Table S2) and 129.2º in the DFT geometry. The largest deviations are observed for the torsion angles. The C1–C2–C3–C4 torsion angle is 169.5º in XRD (Table S2) but only 55.0º in DFT, giving a difference of more than 100º. Similarly, the O11–C13–C14–C15 torsion angle shifts from –6.3º in XRD to 118.3º in the DFT-optimized structure (Table S3).

These differences arise because the crystal lattice locks both the lysinium chain and the adipate backbone into an extended, all-trans conformation, whereas the isolated DFT model, lacking packing constraints, relaxes to a different lower-energy rotamer. Thus, conformational control in the solid state is governed not solely by intrinsic electronic structure but also by crystal packing [26]. The optimized geometry used for the present discussion is shown in Figure. 8.

4.6.2 Frontier Molecular Orbital Analysis

The calculated HOMO-LUMO gap (5.34 eV) is moderate and falls within the range commonly reported for organic acid salts grown for nonlinear optical (NLO) applications [27]. This moderate ΔE (Table 3) is consistent with efficient intramolecular charge transfer (ICT) and microscopic nonlinearity. Related systems, including L-asparagine monohydrate [28] and 2-methylimidazolium hydrogen succinate [29], have also been examined by DFT as part of structure-property and NLO studies. In particular, the relatively low global hardness (η = 2.67 eV) and the higher softness (S = 0.187 eV^{-1}) suggest that LLA is fairly polarizable and capable of rapid intermoiety electron polarization from the protonated lysine donor to the adipate acceptor, in line with the MO isosurface representations showing complementary HOMO and LUMO localization. The high electrophilicity index (ω = 12.75 eV) and ΔN_{max} (3.09) further indicate a strong electron-accepting capacity at the adipate carbonyl region, a feature commonly correlated with second-order NLO response and chemical reactivity in such zwitterionic salts, where intramolecular charge transfer can be inferred from HOMO-LUMO energetics. Collectively, these descriptors support the candidacy of this salt as an NLO-active, moderately stable charge-transfer material. The spatial distributions of the frontier molecular orbitals discussed here are shown in Figure 9.

4.6.3 Mulliken Charge Distribution Analysis

Mulliken population analysis quantifies the charge distribution and its role in the crystal packing of LLA. The carboxylate oxygens O2 (−0.520) and O1 (−0.490) in Table 4 bear large negative charges, identifying them as strong hydrogen-bond acceptors. The protonated lysinium nitrogen N7 (−0.718) and terminal amino nitrogen N1 (−0.609) act as donor centres, and their bonded hydrogens H4 (0.415), H5 (0.411), H23 (0.392), and H24 (0.395) accordingly carry large positive charges.

Table 3. Frontier molecular orbital energies and global chemical reactivity descriptors for LLA computed at B3LYP/6-31+G(d,p)

S No.	Atom	Mulliken Charge	Proposed Role in Crystal Packing
1	O1	-0.519	Strong hydrogen-bond acceptor (carboxylate O)
2	O2	-0.490	Strong hydrogen-bond acceptor (carboxylate O)
3	N3	-0.718	Lysinium protonated N donor center
4	H4	0.414	N–H···O hydrogen-bond donor
5	H5	0.410	N–H···O hydrogen-bond donor
6	N22	-0.609	Protonated amino N donor center
7	H23	0.391	N–H···O hydrogen-bond donor
8	H24	0.395	N–H···O hydrogen-bond donor
9	O26	-0.402	Oxygen participating in O–H···O network
10	O27	-0.167	Protonated O atom of hydrogen adipate involved in O–H···O interaction
11	O42	-0.555	Strong hydrogen-bond acceptor
12	O43	-0.324	Secondary acceptor in O–H···O interaction

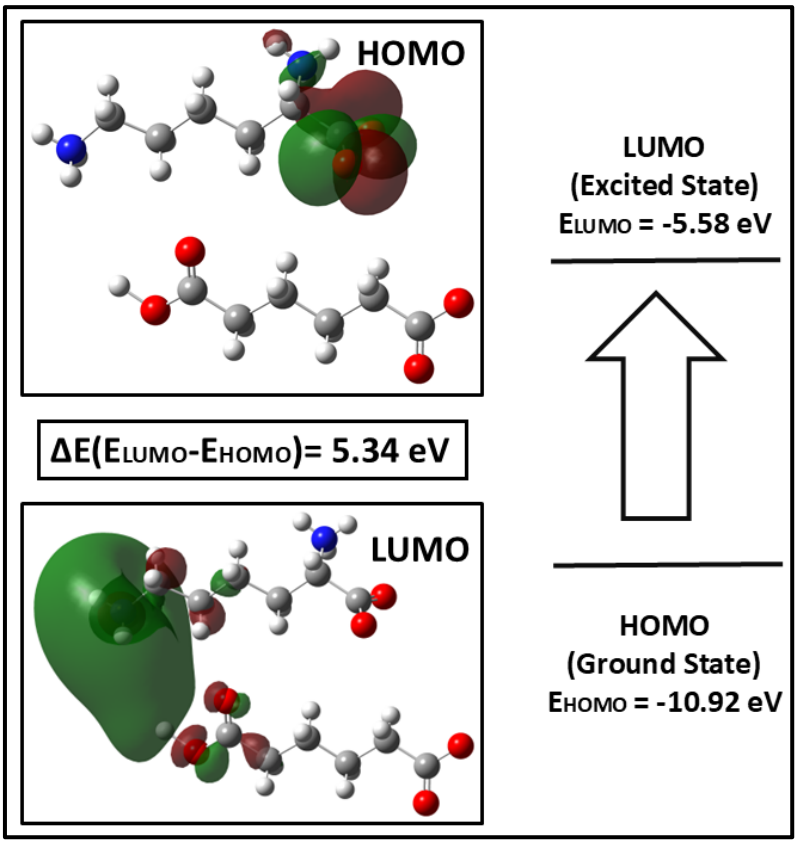

Figure 9. HOMO and LUMO orbitals of LLA molecule with iso-value of 0.02 a.u.

These charge-complementary atom pairs establish strong charge-assisted N–H···O hydrogen bonds directed toward the carboxylate and adipate acceptor oxygens, forming the primary cohesive forces in the crystal lattice [30]. The hydrogen adipate oxygens O20 (−0.402) and O19 (−0.168) participate in O–H···O interactions; the reduced negative charge on O19 is consistent with its role as the proton-bearing oxygen in a near-symmetric O···H···O bridge, generating linear supramolecular chains [31]. The secondary acceptors O11 (−0.555) and O12 (−0.324) further consolidate the three-dimensional network.

Table 4. Selected Mulliken atomic charges of LLA involved in intermolecular hydrogen bonding

Descriptor	Formula	Value
E_{HOMO}	—	−10.92 eV
E_{LUMO}	—	−5.58 eV
Energy gap (ΔE)	$E_{LUMO} - E_{HOMO}$	5.34 eV
Ionization potential (I)	$-E_{HOMO}$	10.92 eV
Electron affinity (A)	$-E_{LUMO}$	5.58 eV
Electronegativity (χ)	(I + A)/2	8.25 eV
Chemical potential (μ)	−(I + A)/2	−8.25 eV
Global hardness (η)	(I − A)/2	2.67 eV
Global softness (S)	1/2η	0.187 eV^{-1}
Electrophilicity index (ω)	$\mu^2/2\eta$	12.75 eV
Max. charge transfer index (ΔN_{max})	−μ/η	3.09

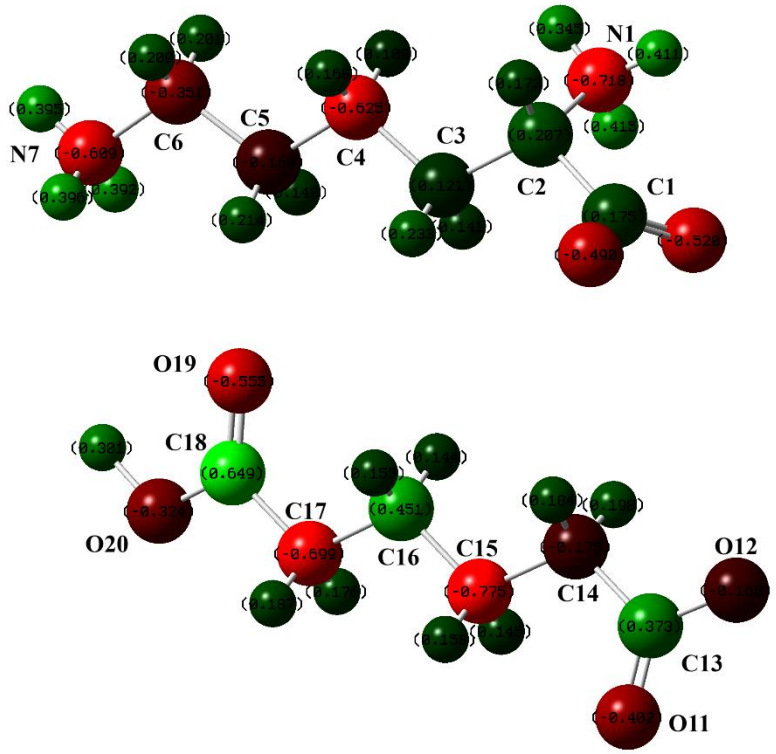

Figure 10. Mulliken atomic charge distribution of LLA.

Collectively, the cooperative N–H···O and O–H···O interactions enforce an NCS polar arrangement within the lattice [32]. This charge-driven, directional hydrogen-bond architecture enhances molecular polarizability and dipole alignment, thereby rationalizing the observed SHG activity of the title crystal [33]. The corresponding Mulliken charge distribution map is shown in Figure 10.

4.6.4 Molecular Electrostatic Potential

The MEP surface of LLA (Figure. 11) maps the electrostatic potential onto the 0.001 a.u. electron-density isosurface and provides a reactivity fingerprint complementary to the FMO picture. Regions of strongly negative potential (deep red, $V_{min} \approx -0.05$ a.u.) are localized over the carboxylate and carboxylic oxygen atoms of adipate, in full agreement with the NBO analysis, which shows that these oxygens carry high lone-pair electron density (occupation 1.59–1.86 e per lone pair). Regions of strongly positive potential (blue, $V_{max} > 0$) envelop the N–H bonds and adjacent methylene protons of lysinium, identifying them as electrophilic sites available for hydrogen-bond donation. The complementarity between the negative MEP sites on one molecule and the positive MEP sites on a neighbouring molecule provides an electrostatic rationale for the observed N–H···O and O–H···O hydrogen bonds in the crystal [34].

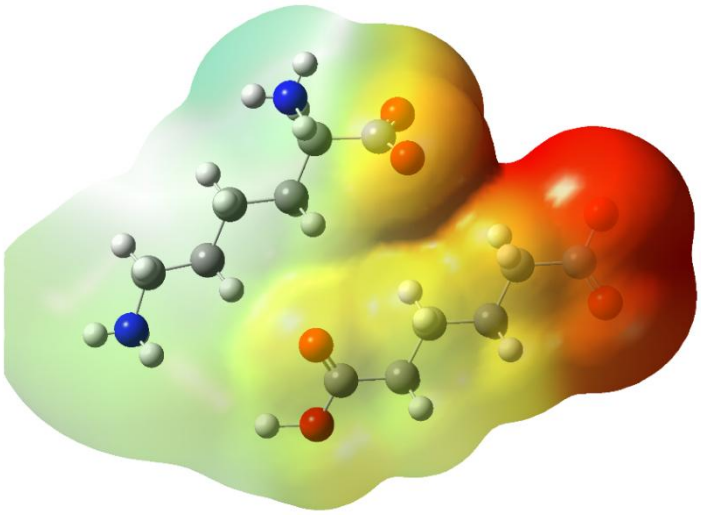

Figure 11. Molecular electrostatic potential surface of LLA mapped onto the 0.001 a.u. electron density isosurface at B3LYP/6-31+G(d,p). The color scale spans −0.05 a.u. (red, electron-rich) to +0.05 a.u. (blue, electron-deficient).

The pronounced MEP anisotropy, with deep red regions at the carboxylate oxygens and blue regions at the ammonium N–H bonds, also explains the large molecular dipole moment of 42.95 D. This degree of electrostatic asymmetry is rarely achieved in non-conjugated organic molecules and is a direct consequence of the zwitterionic ion-pair structure enforced by proton transfer. From a crystal-engineering perspective, the MEP map provides a useful guide for designing co-crystals or salts in which lysinium is paired with different anions: acids whose MEP-positive sites are well matched to the lysinium MEP-negative regions should form stronger hydrogen bonds and potentially better-aligned dipoles for NLO applications [35].

4.6.5 Natural Bond Orbital Analysis

NBO second-order perturbation analysis identifies the orbital-level origin of the charge asymmetry responsible for the NLO response [36]. The interactions are dominated by LP(O) →π*(C–O) and LP (O) →σ*(C–O/C–C) donations concentrated at the carboxylate and carboxylic termini of both ionic species (Table 5). The strongest interaction, LP(3) O2→BD*(2) O1–C1 at 113.03 kcal mol^{-1}, involves the transfer of electron density from a highly occupied oxygen lone pair (1.5916 e) into the low-lying π*-type antibonding orbital of the adjacent carboxylate C=O bond. This type of n→π* interaction is well established as an activating mechanism in zwitterionic amino acid crystals, where it renders each O–C–O fragment electronically asymmetric: the two C–O bonds in the carboxylate become nonequivalent in bond order, creating a polarizable, asymmetric electron distribution that responds efficiently to an applied optical field [37]. The comparable interaction in the adipate anion, LP(3) O19→BD*(2) O20–C13 (67.74 kcal mol^{-1}), and the n→π* donation at the protonated carboxyl terminus, LP(2) O12→BD*(2) C18–O11 (57.15 kcal mol^{-1}), extend this polarization across the full length of the adipate chain, so the NLO-active electron density is not confined to a single terminus but spans the entire anion. Strong-to-moderate interactions (20–30 kcal mol^{-1}) further propagate electronic polarization along the σ-framework through LP(O) →σ*(C–C) and LP(O) →BD*(1) C–O pathways. Although weaker than the principal n→π* interactions, their cumulative effect across multiple bonds extends the charge-transfer distance and increases the ground-state dipole moment, a well-known strategy for enhancing β in donor-π-acceptor organic NLO compounds, here realized in an aliphatic framework through inductive rather than conjugative transmission. The intermolecular LP(1) O11→BD*(1) C3–H3A contact (1.44 kcal mol^{-1}, marked by an asterisk in the table) represents hydrogen-bond-assisted charge transfer from the adipate carbonyl oxygen to a lysinium methylene C–H bond. Despite its modest energy, this interaction is crystallographically directional and contributes to the polar, NCS packing identified by Hirshfeld analysis [38]. Collectively, the NBO analysis demonstrates that the ion-pair architecture of LLA generates a charge-delocalized system that, even in the absence of aromatic or vinyl π-conjugation, achieves a hyperpolarizability competitive with extended conjugated systems through the combined action of multiple strong LP→π*/σ* donations and substantial interionic charge transfer.

4.6.6 Dipole Moment, Polarizability, and First Hyperpolarizability

The computed molecular dipole moment, polarizability tensor, and first hyperpolarizability components of LLA are collected in Table 6.

Table 5. Selected second-order perturbation NBO interactions for LLA at B3LYP/6-31+G(d,p), grouped by stabilization energy. $E^{(2)}$: hyperconjugative stabilization; E(j)−E(i): donor–acceptor NBO energy difference; F(i,j): Fock matrix element. Asterisk (*) denotes intermolecular interaction

Donor (i)	ED(i) /e	Acceptor (j)	ED(j) /e	(E^{-2}) (kcal mol^{-1})	E(j)−E(i) /a.u.	F(i,j) /a.u.
Very strong interactions — (E^{-2}) > 50 kcal mol^{-1} (principal NLO-active pathways)						
LP(3) O2	1.591	BD*(2) O1–C1	0.395	113.03	0.27	0.157
LP(3) O19	1.663	BD*(2) O20–C13	0.324	67.74	0.34	0.136
LP(2) O12	1.801	BD*(2) C18–O11	0.235	57.15	0.35	0.128
Strong interactions — (E^{-2}) = 20–50 kcal mol^{-1}						
LP(2) O11	1.862	BD*(1) C18–O12	0.087	30.59	0.70	0.132
LP(2) O20	1.791	BD*(1) O19–C13	0.061	28.23	0.81	0.140
LP(2) O1	1.850	BD*(1) C1–C6	0.129	27.27	0.55	0.110
LP(2) O2	1.862	BD*(1) C1–C6	0.129	26.05	0.57	0.109
Intermolecular hydrogen-bond-assisted charge transfer						
LP(1) O11	1.972	BD*(1) C3–H3A	0.018	1.44	1.32	0.039

Table 6. Computed electric dipole moment (μ), polarizability (α), and first hyperpolarizability (β) components of LLA at B3LYP/6-31+(d,p)

α component	Value (×10^{-24} esu)	β component	Value (×10^{-33} esu)
α_{xx}	186.75	β_{xxx}	−119508.12
α_{xy}	−1.96	β_{xxy}	31002.80
α_{yy}	25.89	β_{xyy}	−64959.46
α_{xz}	53.60	β_{yyy}	6987.96
α_{yz}	−0.21	β_{xxz}	−115023.32
α_{zz}	56.11	β_{xyz}	12783.91
α_0 (mean)	89.58	β_{yyz}	−43955.97
μ_x	−42.88 D	β_{xzz}	−12.57
μ_y	−1.10 D	β_{yzz}	1438.47
μ_z	−2.31 D	β_{zzz}	−136684.34
μ_0	42.95 D	β_{total}	460794.38

The scalar dipole moment μ_0 = 42.95 D, with the dominant component along x (μ_x = −42.88 D), confirms that charge polarization is strongly axial, a geometry that maximizes the projection of the molecular dipole onto the polar crystal axis and thereby enhances bulk $\chi^{(2)}$ through the additive superposition of unit-cell contributions. This dipole magnitude is exceptional for a non-conjugated organic molecule and reflects the near-integer formal charges of the lysinium cation (+1) and adipate anion (−1), modulated by covalent delocalization to an effective interionic transfer of approximately 0.31e (natural population charges +0.691 and −0.691 rather than formal ±1). The mean polarizability $\alpha_0 \approx 89.58 \times 10^{-24}$ esu and the polarizability anisotropy $\Delta\alpha \approx 174.8 \times 10^{-24}$ esu describe an electron cloud that deforms strongly and anisotropically under an applied field; both properties are prerequisites for a large hyperpolarizability. The computed β_{total} = 460794.38 × 10^{-33} esu is approximately 795 times the β of urea (0.58 × 10^{-33} esu). The dominant negative contributions to β are concentrated in the x and z tensor components (β_{xxx} = −119508, β_{xxz} = −115023 and β_{zzz} = −136684 × 10^{-33} esu), consistent with directional charge transfer along the molecular x-axis defined by the $NH3^{+}\cdots OOC$ vector [39]. The magnitude of β_{total} is remarkable for a compound without any aromatic ring and underscores that ionic charge separation, when combined with strong LP→π*/σ* orbital interactions and a rigid, acentric crystal

architecture, can match or surpass extended-conjugation strategies for second-order NLO performance [40]. The agreement between the high computed β and the measured 1.2 × KDP SHG efficiency is internally consistent: the Kurtz-Perry technique samples a powder average ($\beta_{eff} \approx \beta_{total}/5$ for an isotropic powder), and the resulting powder SHG response correlates well with the DFT-predicted tensor magnitude.

4. Conclusion

L-lysinium hydrogen adipate single crystals were grown by slow evaporation and characterized through a combination of structural, spectroscopic, thermal, optical, and computational methods. SCXRD confirmed the NCS monoclinic $P2_1$ structure, a prerequisite for SHG, with unit-cell parameters in excellent agreement with literature values. Hirshfeld surface analysis further established that the crystal packing is sustained by an extensive network of N–H···O and O–H···O hydrogen bonds (45.8% of the Hirshfeld surface area), which enforce acentric symmetry and provide the mechanical and thermal rigidity necessary for device operation. Quantum-chemical analysis at the B3LYP/6-31+G(d,p) level revealed a HOMO-LUMO gap of 5.34 eV arising from a spatially separated donor (lysinium NH_3^+/carboxylate) and acceptor (adipate carboxylate) pair. NBO second-order perturbation analysis identified LP(3) O1→BD*(2) O2–C7 (113.03 kcal mol^{-1}) and analogous n→π* pathways at the adipate termini as the principal charge-transfer interactions underpinning the NLO response. The calculated first hyperpolarizability of 460.79 × 10^{-30} esu (approximately 795 × that of urea) demonstrates that ionic proton-transfer salts can achieve hyperpolarizabilities rivalling those of extended π-conjugated chromophores. The measured Kurtz-Perry SHG efficiency of 1.2 × KDP is consistent with this computational prediction. LLA exhibits thermal stability up to 150 ºC and a sharp melting endotherm at 203 ºC, features that are favourable for photonic-device applications. Finally, replacing adipate with longer-chain or branched diacids offers a straightforward synthetic route for systematically tuning the supramolecular geometry and β, guided by the MEP-based design principles established here. Overall, LLA represents a viable, synthetically accessible, and crystallographically well-defined platform for second-order photonic applications, and the structure-property framework developed in this study provides a rational basis for optimizing analogous proton-transfer salts.

References

[1] A. Boes, L. Chang, C. Langrock, M. Yu, M. Zhang, Q. Lin, M. Lončar, M. Fejer, J. Bowers, A. Mitchell, Lithium Niobate Photonics: Unlocking the Electromagnetic Spectrum. Science, 379, (2023) eabj4396. https://doi.org/10.1126/science.abj4396

[2] S. Feng, S. Wu, W. Zhang, F. Liu, J. Wang, Organic Electro-Optic Materials with High Electro-Optic Coefficients and Strong Stability. Molecules, 29, (2024) 3188. https://doi.org/10.3390/molecules29133188

[3] H. Wang, L. Chen, Y. Wu, Advancing Inorganic Electro-Optical Materials for 5G Communications: From Fundamental Mechanisms to Future Perspectives. Light: Science & Applications, 14, (2025) 190. https://doi.org/10.1038/s41377-025-01851-9

[4] H. Jia, B. Chen, F. Zhang, X. Hou, S. Pan, The Condensation of π-Conjugated Units: A New Paradigm for Designing High-Performance Optical Crystals. Chemical Society Reviews, 55(10), (2026) 5838–5866. https://doi.org/10.1039/D5CS01327E

[5] E. Mohanapriya, S. Thennarasu, S. Devanesan, M.A. Wadaan, N. Kanagathara, J. Janczak, Crystal Engineering Perspective on Supramolecular Architecture and Electronic Properties of adeninium 5-sulfoisophthalate via Hirshfeld and DFT Analysis. Journal of Molecular Structure, 1370, (2026) 146429. https://doi.org/10.1016/j.molstruc.2026.146429

[6] J.J.L.M. Cornelissen, A.E. Rowan, R.J.M. Nolte, N.A.J.M. Sommerdijk, Chiral Architectures from Macromolecular Building Blocks. Chemical Reviews, 101(12), (2001) 4039–4070. https://doi.org/10.1021/cr990126i

[7] S. Debrus, M.K. Marchewka, J. Baran, M. Drozd, R. Czopnik, A. Pietraszko, H. Ratajczak, L-Lysine-L-tartaric acid: New Molecular Complex with Nonlinear Optical Properties. Structure, Vibrational Spectra and Phase Transitions. Journal of Solid State Chemistry, 178(9), (2005) 2880–2896. https://doi.org/10.1016/j.jssc.2005.06.029

[8] V. Vasudevan, N. Renuka, R. Ramesh Babu, K. Ramamurthi, Growth, Spectral, Thermal, Optical, Mechanical and Etching Studies of L-Lysine Semi-Maleate (L-LSM) single crystals. Spectrochimica Acta Part A: Molecular and Biomolecular Spectroscopy, 136, (2015) 1850–1856. https://doi.org/10.1016/j.saa.2014.10.095

[9] M. Byres, P.J. Cox, G. Kay, E. Nixon, Supramolecular Structures of Six Adenine-Carboxylic Acid Complexes. CrystEngComm, 11(1), (2009) 135–142. https://doi.org/10.1039/B811243F

[10] A. Sharma, S. Thamotharan, S. Roy, M. Vijayan, X-ray Studies of Crystalline Complexes involving Amino Acids and Peptides. XLIII. Adipic Acid Complexes of L- and DL-lysine. Acta Crystallographica Section C, 62(3), (2006) o148–o152. https://doi.org/10.1107/S0108270106003374

[11] M. Mutailipu, J. Li, S. Pan, Looking Back the Nonlinear Optical Crystals in a Functionalized Unit's Perspective. Advanced Functional Materials, 35(16), (2025) 2419204. https://doi.org/10.1002/adfm.202419204

[12] D.J. Clark, J.-H. Zhang, A.J. Craig, A. Weiland, J.A. Brant, J.B. Cho, Y.S. Kim, J.I. Jang, J.A. Aitken, The Kurtz-Perry Powder Technique Revisited: A Case Study on the Importance of Reference Quality and Broadband Nonlinear Optical Measurements using LiInSe2. Journal of Alloys and Compounds, 917, (2022) 165381. https://doi.org/10.1016/j.jallcom.2022.165381

[13] M.J. Frisch, G.W. Trucks, H.B. Schlegel, G.E. Scuseria, M.A. Robb, J.R. Cheeseman, G. Scalmani, V. Barone, B. Mennucci, G.A. Petersson, H. Nakatsuji, (2009). Gaussian 09, Revision D.01. Gaussian, Inc., Wallingford, CT. https://gaussian.com/

[14] R. Dennington, T.A. Keith, J.M. Millam, (2016) GaussView, Version 6.1. Semichem Inc., Shawnee Mission.

[15] S. Horiuchi, S. Ishibashi, Hydrogen-Bonded Small-Molecular Crystals Yielding Strong Ferroelectric and Antiferroelectric Polarizations. Journal of the Physical Society of Japan, 89(5), (2020) 051009. https://doi.org/10.7566/JPSJ.89.051009

[16] J. Alongi, A. Beduini, E. Ranucci, Mechanistic Insights into the Thermal Decomposition of Linear Polyamidoamines via Coupled TG–FTIR analysis. Polymer Degradation and Stability, 250, (2026) 112212. https://doi.org/10.1016/j.polymdegradstab.2026.112212

[17] K. Ramya, N.T. Saraswathi, C. Ramachandra Raja, Growth and Characterization of L-Lysine Adipate crystal. Optics & Laser Technology, 90, (2017) 222–225. https://doi.org/10.1016/j.optlastec.2016.12.002

[18] J. Lin, K. Du, H. Jiang, Large-Sized Organic Semiconductors: Crystallization, Characterization and Applications. CrystEngComm, 27(25), (2025) 4243–4257. https://doi.org/10.1039/D5CE00398A

[19] R. Thirumurugan, S. Priyadharshini, B. Babu, B. Mohan Babu, K. Anitha, An Efficient Phase Matching Second Harmonic Generation of 2-amino-4-Methylpyridinium Quinoline-2-carboxylate (C16H15N3O2) Organic Single Crystal: Structural, Optical, Thermal, and Computational Investigations. Journal of Molecular Structure, 1332, (2025) 141453. https://doi.org/10.1016/j.molstruc.2025.141453

[20] M. Springborg, Chemical Modelling: Applications and Theory Volume. Royal Society of Chemistry, 6, (2009) 17–62.

[21] J. Qian, Y. Wang, J. Ding, X. Su, Q. Wu, Breaking the SHG-Stability Trade-Off in UV Nonlinear Optical Materials by Polar-Layer-Dense-Locking. Chemical Science, 17(27), (2026) 13691-13698. https://doi.org/10.1039/D6SC03803D

[22] P. Sahoo, Introducing Dihedral Angle Torsion in a Flexible Dicarboxylic Acid: Evolution from a Sequential Symmetry Condensing Liquid Crystalline Gel to a Step-Halting Heat-Set Gel. Crystal Growth & Design, 24(8), (2024) 3100–3108. https://doi.org/10.1021/acs.cgd.4c00160

[23] P.R. Spackman, M.J. Turner, J.J. McKinnon, S.K. Wolff, D.J. Grimwood, D. Jayatilaka, M.A. Spackman, CrystalExplorer: A program for Hirshfeld Surface Analysis, Visualization and Quantitative Analysis of Molecular Crystals. Journal of Applied Crystallography, 54, (2021) 1006–1011. https://doi.org/10.1107/S1600576721002910

[24] R. Thirumurugan, B. Babu, K. Anitha, J. Chandrasekaran, Experimental and Computational Perspectives on Bis(creatininium) Succinate: An Efficient Organic Nonlinear Optical Material. Zeitschrift für Physikalische Chemie, 231(11–12), (2017) 1849–1874. https://doi.org/10.1515/zpch-2016-0896

[25] M. Sliwa, S. Létard, I. Malfant, M. Nierlich, P.G. Lacroix, T. Asahi, H. Masuhara, P. Yu, K. Nakatani, Design, Synthesis, Structural and Nonlinear Optical Properties of Photochromic Crystals: Toward Reversible Molecular Switches. Chemistry of Materials, 17(18), (2005) 4727–4735. https://doi.org/10.1021/cm050929o

[26] R. Thirumurugan, B. Babu, K. Anitha, Exploring Second-Order NLO Activity in Imidazolium Quinoline-2-Carboxylate Dihydrate (IQD): Synthesis, Crystal Engineering, Spectral and DFT Insights. Journal of Molecular Structure, 1351, (2026) 144130. https://doi.org/10.1016/j.molstruc.2025.144130

[27] N.A. Mohamad Daud, Q.A. Wong, B.S. Ooi, C.K. Quah, F.D. Ramzi, Y.-F. Win, P.S. Patil, Impact of Homocyclic and Heterocyclic Rings of Chalcones on Charge Transfer Behaviour: A nonlinear optical study. Chemical Physics Impact, 8, (2024) 100565. https://doi.org/10.1016/j.chphi.2024.100565

[28] W.D. Arnold, L.K. Sanders, M.T. McMahon, A.V. Volkov, G. Wu, P. Coppens, S.R. Wilson, N. Godbout, E. Oldfield, Experimental, Hartree–Fock, and Density Functional Theory Investigations of the Charge Density, Dipole Moment, Electrostatic Potential, and Electric Field Gradients in L-Asparagine Monohydrate. Journal of the American Chemical Society, 122(19), (2000) 4708–4717. https://doi.org/10.1021/ja000386d

[29] K. Sowmiya, S. Arokiyasamy, M. Avinash, R. Gunaseelan, P. Sanjay, 2-Methylimidazolium Hydrogen Succinate Single Crystal Growth and

DFT Insight for NLO Applications. Molecular Physics, 123, (2025) e2486660. https://doi.org/10.1080/00268976.2025.2486660

[30] P. Rodríguez-Cuamatzi, O.I. Arillo-Flores, M.I. Bernal-Uruchurtu, H. Höpfl, Experimental and Theoretical Analysis of the hydrogen-Bonding Motifs formed between the Carboxyl and the Carboxylate Group: Towards a Systematic Classification of their Supramolecular Motifs. Supramolecular Chemistry, 19(8), (2007) 559–578. https://doi.org/10.1080/10610270701474439

[31] P. Devi, P.T. Muthiah, T.N. Guru Row, V. Thiruvenkatam, Hydrogen bonding in Pyrimethamine Hydrogen Adipate. Acta Crystallographica Section E, 63(10), (2007) o4065–o4066. https://doi.org/10.1107/S1600536807044364

[32] L. Liao, C.W. Ingram, J. Bacsa, Z.J. Zhang, T. Dinadayalane, A Hydrogen Bonded Co(II) Coordination Complex and a Triply Interpenetrating 3-D Manganese(II) Coordination Polymer from Diaza Crown ether with Dibenzoate Sidearms. CrystEngComm, 18(14), (2016) 2425–2436. https://doi.org/10.1039/C6CE00360E

[33] M.-C. Wang, J.-J. Li, Y. Chen, K.-Z. Du, J. Chen, Organic Halogen Substitution-Driven Halogen Bonding Induces Polar 3D Supramolecular Framework and Second-Harmonic-Generation Response. Inorganic Chemistry, 64(38), (2025) 19157–19163. https://doi.org/10.1021/acs.inorgchem.5c03877

[34] R. Thirumurugan, K. Anitha, Experimental and Theoretical Investigations on a Hydrous Organic Salt of 2, 4, 6-Triaminopyrimidine-1, 3-diium L-Tartrate Monohydrate (TTM). Journal of Molecular Structure, 1237, (2021) 130368. https://doi.org/10.1016/j.molstruc.2021.130368

[35] Z. Wang, X. Jiang, X. Wang, K. Duanmu, L. Bai, C. Wu, Z. Lin, Z. Huang, M.G. Humphrey, C. Zhang, A Deep-Ultraviolet Transparent Nonlinear Optical Hydrogen-Bonded Organic Framework. Journal of the American Chemical Society, 148(1), (2026) 135–140. https://doi.org/10.1021/jacs.5c19874

[36] [36] M. Mutailipu, J. Li, S. Pan, Looking Back the Nonlinear Optical Crystals in a Functionalized Unit's Perspective. Advanced Functional Materials, 35(16), (2025) 2419204. https://doi.org/10.1002/adfm.202419204

[37] A. El-Ghayoury, C. Mézière, S. Simonov, L. Zorina, M. Cobián, E. Canadell, C. Rovira, B. Náfrádi, B. Sipos, L. Forró, P. Batail, A Neutral Zwitterionic Molecular Solid. Chemistry – A European Journal, 16, (2010) 14051–14059. https://doi.org/10.1002/chem.201001875

[38] S. Vishnoi, S. Guerin, Predicting and Rationalizing Piezoelectricity in Racemic Bioorganic Molecular Crystals. Angewandte Chemie International Edition, 65(26), (2026) e24346. https://doi.org/10.1002/anie.202524346

[39] M. Majumder, A. Misra, Strategic Design of Thiophene-Fused Nickel Dithiolene Derivatives for Efficient NLO Response. Physical Chemistry Chemical Physics, 20(28), (2018) 19007–19016. https://doi.org/10.1039/C8CP01592A

[40] M. Ibrahim, A. Yousuf, M.Z. Qureshi, M. Arshad, M.A. Ali, Disentangling Solvent effects on Optical response via p-π and sp² Lone-Pair Contributions in Non-Aromatic Fused Systems. Scientific Reports, 16(1), (2026) 10935. https://doi.org/10.1038/s41598-026-44846-1

Authors Contribution Statement

R. Thirumurugan: Conceptualization, Methodology, Data curation, Formal analysis, Validation, Writing - Original Draft, Writing – review and editing. Srirengaraj Vijayaram: Writing - Original Draft, Writing - Review & Editing. E. Shobhana: Writing - Original Draft, Writing - Review & Editing. Mohanraj: Writing - Original Draft, Writing - Review & Editing. All the authors have read and agreed to the published version of the manuscript.

Funding

The authors declare that no funds, grants or any other support were received during the preparation of this manuscript.

Competing Interests

The authors declare that there are no conflicts of interest regarding the publication of this manuscript.

Data Availability

The data supporting the findings of this study can be obtained from the corresponding author upon reasonable request.

Has this article screened for similarity?

Yes